Contributions of bulk and surface energies in stabilizing metastable polymorphs: A comparative study of group 3 sesquioxides La_2O_3, Ga_2O_3, and In_2O_3

Fatima Al-Quaiti,[1] P.-Y. Chen,[2] J. G. Ekerdt,[2] and A. A. Demkov [3,*]

[1]*Department of Chemistry, The University of Texas, Austin, Texas 78712, USA*
[2]*Department of Chemical Engineering, The University of Texas, Austin, Texas 78712, USA*
[3]*Department of Physics, The University of Texas, Austin, Texas 78712, USA*

Sesquioxides are an important class of compounds which are used in various applications such as optical glasses, high-power electronics, and gate dielectrics. Using density functional theory, we investigated bixbyite La_2O_3, In_2O_3, and Ga_2O_3; hexagonal La_2O_3; corundum In_2O_3; and monoclinic Ga_2O_3. We compared the predicted structural properties for each material using the local density approximation (LDA) and the generalized-gradient approximation [GGA PBE (Perdew-Burke-Ernzerhof)]. We found that LDA predicts the correct ground state structure for all three sesquioxides; however, GGA PBE predicts the incorrect ground state structure for La_2O_3. To gain better insight on why this happens, we calculated the phonon properties and the free energy for all structures to determine phase transition temperatures. Additionally, we determined the transition pressure for In_2O_3. We also studied several surface terminations for each compound and determined the lowest-energy surface for each structure as well as the interfacial energy for La_2O_3.

I. INTRODUCTION

Sesquioxides are compounds with the chemical structure M_2O_3 in which M is a metal atom. They are an important group of oxides that can be used as conductors, semiconductors, and insulators. La_2O_3, In_2O_3, and Ga_2O_3 all have a similar chemical formula with metal atoms possessing a 3+ valence charge. However, they have different electronegativities and ionic radii with La being the least electronegative and largest ion and Ga being the most electronegative and smallest ion. These differences result in the sesquioxides having different ground state structures, conductivity, and band gaps, which opens the possibility for tuning materials through alloying. By alloying these materials, one can tune physical properties such as the conductivity, optical and electronic band gaps, and phase stability, which can be optimized for use in high-frequency and high-power applications [1]. However, there are some issues with alloying these materials such as phase separation, unpredictability of the phase that will form, and structural instability [1]. To understand how these alloys will form, a thorough understanding of ground state and metastable structures is essential.

La_2O_3 is a rare earth metal oxide used for nonvolatile memory [2], thin-film transistors [2], and optical glasses [3–5]. Additionally, La_2O_3 has potential as a high-k gate dielectric in metal-oxide-semiconductor (MOS) devices due to its wide band gap of $\sim 5\,eV$ and dielectric constant k of ~ 27 [2]. One of the main challenges with La_2O_3 is its hygroscopic nature. Some treatments for this are annealing with O_2 to reduce the amount of lanthanum carbonate [6], doping La_2O_3 with a second metal element such as Y, Ta, and Nb [2], and postde-

position ultraviolet ozone treatment [2]. A second challenge with La_2O_3 is the presence of defects in the bulk and interface with Si, which lowers the effective k value and causes charge trapping [2]. Higher-quality films are necessary to reduce the interface trap density [6]. Hence, a thorough understanding of La_2O_3 is necessary to determine how to treat the surface and prepare it for use as a gate dielectric.

The ground state structure of La_2O_3, shown in Fig. 1(a), is the hexagonal phase (A-La_2O_3) (space group $P\bar{3}m1$), which has five atoms in the unit cell with sevenfold coordinated La atoms surrounded by two types of O atoms with fourfold (O1) and sixfold coordination (O2) [2]. During thin film growth on GaN (0001), the metastable bixbyite phase (C-La_2O_3) (space group $Ia\bar{3}$), shown in Fig. 1(b), forms when the film is below a certain thickness, called the critical thickness, when grown in layer by layer fashion [7,8] and sometimes forms polymorphic films with A-La_2O_3 [9]. This could be a result of surface energy considerations. While the energy of bulk A-La_2O_3 is lower than that of C-La_2O_3, if the surface energy of A-La_2O_3 is higher than that of C-La_2O_3, the cubic phase may be stabilized when the film thickness is below the critical thickness. The surface energy can play an important role in stabilizing the phase with higher bulk energy. If the surface area is relatively large compared to the bulk region, then the low energy of the surface may dictate the phase of the material rather than the lower-energy bulk structure. Using computational methods, we can determine the bulk energy and lowest-energy surface termination for each phase and predict the critical thickness.

In_2O_3 is a semiconducting oxide that is often used as a transparent conducting oxide (TCO) when doped with Sn or Ti. While In_2O_3 can be used as a semiconductor, growing high-quality In_2O_3 films remains a challenge due to unintentional doping or intrinsic point defects [10]. Since TCOs

*demkov@physics.utexas.edu

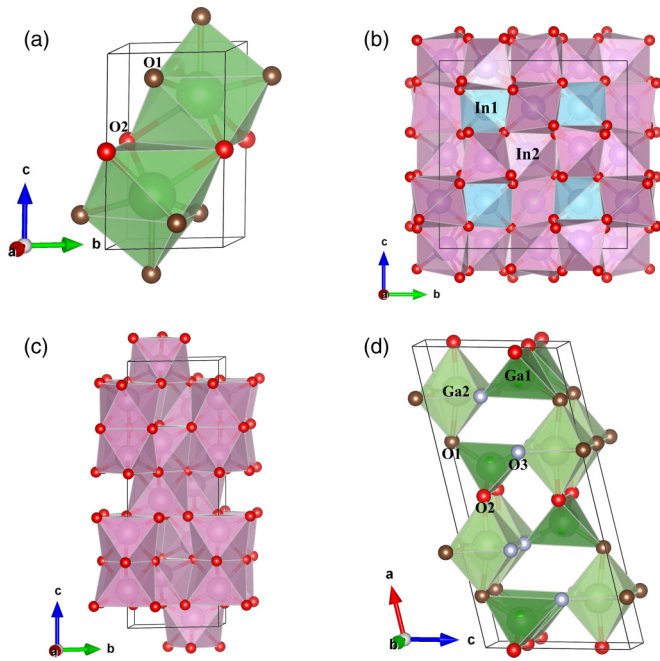FIG. 1. Bulk structures of (a) hexagonal La_2O_3, (b) the bixbyite phase, (c) corundum In_2O_3, and (d) monoclinic Ga_2O_3.

do not require high-quality films, doped polycrystalline In_2O_3 films are used as TCOs. Recently, interest in using In_2O_3 as a semiconductor has been renewed because it can be used in transparent electronics and improve applications such as gas sensors or transparent contacts. To improve crystal quality and understand how to apply In_2O_3 in semiconductor applications, we need to better understand its bulk and surface properties, which affect band bending, carrier concentration, the Seebeck coefficient, and conductivity [10].

At ambient temperatures and pressures, In_2O_3 exists in the bixbyite phase (C-In_2O_3), shown in Fig. 1(b). The bixbyite structure has 80 atoms in the unit cell with one-fourth of the In^{3+} ions occupying trigonally compressed octahedral sites (In1), three-quarters occupying distorted octahedral sites (In2), and both surrounded by fourfold coordinated O^{2-} ions. At high pressures and high temperatures, In_2O_3 transforms to the corundum phase (rh-In_2O_3) (space group $R\bar{3}c$) [11], shown in Fig. 1(c) and more recent studies show rh-In_2O_3 can be synthesized in ambient conditions [12–14]. The corundum structure has 30 atoms in the conventional unit cell with O^{2-} ions occupying a hexagonal close packed arrangement and In^{3+} ions occupying two-thirds of the available octahedral sites. C-In_2O_3 is well studied due to its use as a TCO; however, some studies suggest that rh-In_2O_3 may perform better as a TCO due to its higher conductivity and more stable capacity [11,15,16], necessitating more studies on bulk and surface properties of rh-In_2O_3.

Ga_2O_3 is an ultrawide band gap semiconductor with potential applications in high-power electronic devices, solar-blind ultraviolet photodetectors, and electro-optical devices [1]. Recently, 2- and 4-in. wafers of β-Ga_2O_3 have been synthesized using the Czochralski method and edged-defined film-fed growth method, respectively. This has led to a rise in studies of β-Ga_2O_3 due to its potential use in commercial applications

such as Ga_2O_3-based field effect transistors, Schottky barrier diodes, and solar-blind UV detectors. Ga_2O_3-based applications still face several challenges due to limited control over impurities and defects and a need for better understanding of unintentional defects, deep level trap states, and carrier transport mechanisms.

The ground state structure of Ga_2O_3 is the monoclinic structure (space group $C2/m$), shown in Fig. 1(d), denoted β-Ga_2O_3. There are 20 atoms in the β-Ga_2O_3 conventional unit cell with Ga^{3+} ions occupying distorted octahedral (Ga1) and tetrahedral sites (Ga2) and O^{2-} ions (O1, O2, and O3) occupying three inequivalent sites in a distorted cubic close-packed arrangement. Ga_2O_3 has several polymorphs including α-Ga_2O_3, γ-Ga_2O_3, δ-Ga_2O_3, and κ-Ga_2O_3. The α-Ga_2O_3 phase is a rhombohedral structure with the $R\bar{3}c$ space group and is analogous to the corundum structure. γ-Ga_2O_3 is a cubic structure with space group $Fd\bar{3}m$. The δ-Ga_2O_3 phase, which we will denote as C-Ga_2O_3 throughout this work, was first identified by Roy *et al.* [17] as the bixbyite structure. However, it has been suggested that, rather than a distinct polymorph, C-Ga_2O_3 is a form of ε-Ga_2O_3, which is an orthorhombic phase with space group $Pna2_1$ [1,18]. However, when alloying Ga_2O_3 with In_2O_3, the $In_xGa_{1-x}O_3$ alloy can exist in both the bixbyite and monoclinic phases [1]. Hence, it is important to understand the C-Ga_2O_3 phase to understand how it can incorporate into C-In_2O_3. Monoclinic Ga_2O_3 has low crystallographic symmetry, which leads to anisotropy of the physical, optical, and electrical properties of Ga_2O_3. Hence, a thorough understanding of the surface arrangement for different β-Ga_2O_3 terminations is necessary to investigate how physical properties differ for each of the experimentally observed surface terminations.

In this work, we study the surface energy for various surface terminations of several key polymorphs for each of the three sesquioxides and compare the results when using different exchange correlation functionals. To explore the effects that the surface energy may have on the phase observed during thin film growth, we use first principles calculations to study the bixbyite phases of La_2O_3, In_2O_3, and Ga_2O_3 and the hexagonal, corundum, and monoclinic phases of La_2O_3, In_2O_3, and Ga_2O_3, respectively. We have calculated the cohesive energies using local density approximation (LDA) and generalized-gradient approximation (GGA)–Perdew-Burke-Ernzerhof (PBE) exchange correlation functionals, the free energies using phonon properties for each compound, and the energy of several surface terminations for each material in the ground and metastable phases.

II. METHODS

Density functional theory (DFT), as implemented in the Vienna *ab initio* simulation package (VASP) code, is used to perform all calculations [19]. The Perdew-Burke-Ernzerhof (PBE) generalized-gradient approximation (GGA PBE) and local density approximation (LDA) were used for the exchange correlation energy functional. We use projector-augmented-wave potentials [20] to describe La, In, Ga, and O with valence electron configurations $5s^25p^66s^25d^1$ for La, $4d^{10}5s^25p^1$ for In, $3d^{10}4s^24p^1$ for Ga, and $2s^22p^4$ for O. For all calculations, each self-consistent electronic calculation is

converged to within 10^{-6} eV per cell, and the ionic relaxation is iterated until the forces are less than 0.01 eV/Å.

A $5 \times 5 \times 5$ k-point grid was used for structural optimization of bulk structures bixbyite La_2O_3, In_2O_3, and Ga_2O_3 (space group $Ia\bar{3}$). For hexagonal La_2O_3 (space group $P\bar{3}m1$), corundum In_2O_3 (space group $R\bar{3}c$), and monoclinic Ga_2O_3 (space group $C2/m$), $9 \times 9 \times 6$, $9 \times 9 \times 3$, and $5 \times 19 \times 11$ k-point grids were used, respectively. To perform density of states (DOS) calculations, each k-point grid was increased by 2 along each direction. Additionally, structural optimizations of bulk La (space group $P6_3/mmc$), bulk In (space group $I4/mmm$), and bulk Ga (space group $Abma$) were performed using $8 \times 8 \times 6$, $9 \times 9 \times 3$, and $10 \times 10 \times 8$ grids, respectively. A 500 eV energy cutoff was used for all bulk calculations. To calculate the phonon properties, we employed the finite displacement using VASP and calculated the phonon dispersion and DOS using the PHONOPY package [21]. For bulk phonon calculations, we used $2 \times 2 \times 1$, $3 \times 3 \times 2$, and $1 \times 4 \times 2$ supercells of rh-In_2O_3, A-La_2O_3, and β-Ga_2O_3, respectively, and one unit cell for all bixbyite structures.

To investigate the surface properties of the La_2O_3, In_2O_3, and Ga_2O_3 surfaces, we used slabs at least 10 Å thick with at least 10 Å of vacuum to ensure adequate separation between surfaces. A 600 eV energy cutoff was used to optimize the structure of the slabs along with the same electronic and ionic convergence criteria used for the bulk structures. We studied the (001), (011), and (111) surfaces for bixbyite phases using $(5 \times 5 \times 1)$, $(5 \times 3 \times 1)$, and $(5 \times 5 \times 1)$ k-point grids, respectively. Additionally, we studied the (001), (110), (100), and (1$\bar{1}$2) surfaces for hexagonal La_2O_3 using $(9 \times 9 \times 1)$, $(6 \times 6 \times 1)$, $(5 \times 5 \times 1)$, and $(3 \times 9 \times 1)$ grids, respectively. Similarly, the (001), (110), (100), and (1$\bar{1}$2) surfaces for corundum In_2O_3 were studied using $(9 \times 9 \times 1)$, $(6 \times 8 \times 1)$, $(8 \times 3 \times 1)$, and $(8 \times 8 \times 1)$ k-point grids, respectively. For monoclinic Ga_2O_3 (100), (11$\bar{2}$), ($\bar{2}$01), (310), and (101) surfaces were studied using $(5 \times 9 \times 1)$, $(5 \times 7 \times 1)$, $(7 \times 7 \times 1)$, $(5 \times 7 \times 1)$, and $(5 \times 25 \times 1)$ k-point grids, respectively.

III. RESULTS AND DISCUSSION

A. Bulk properties

We start by computing the bulk properties and, where possible, compare our computed values with experiment. The lattice constants calculated for each bulk structure are reported in Table I. For all structures except rh-In_2O_3, the lattice constants determined using GGA PBE more favorably matched experimentally determined lattice constants. The lattice constants calculated using LDA and GGA PBE favorably match previously reported theoretical values for bulk La [22], A-La_2O_3 [22–24], C-La_2O_3 [25], rh-In_2O_3 [26–29], C-In_2O_3 [26,27,29], β-Ga_2O_3 [29–32], and C-Ga_2O_3 [29,31].

The formation energies for the La_2O_3, In_2O_3, and Ga_2O_3 phases are also reported in Table I. The formation energy is a measure of the internal energy of a material and a lower (more negative) formation energy indicates a more stable structure. When using GGA PBE, we found the theoretical formation energies for all three oxides were higher than what was measured experimentally [33]. The formation energies determined using GGA PBE indicate C-La_2O_3 is more stable

than A-La_2O_3, which is not observed in experiment. On the other hand, the formation energies calculated with LDA match experimental values [33] very well and correctly predict the correct ground state structure is A-La_2O_3. The formation energies calculated using both GGA PBE and LDA predict the correct ground state structures are C-In_2O_3 and β-Ga_2O_3, which supports experimental observations. Overall, the LDA functional predicts formation energy values that match more closely to experiment and may be more suitable for energetic studies of these sesquioxides.

The calculated band gaps of all three sesquioxides, listed in Table I, are underestimated using both GGA PBE (Fig. 2) and LDA (Fig. 3), which is typical for these methods. We determine a band gap of 3.93 eV using GGA PBE and 3.74 eV using LDA for A-La_2O_3, which compare favorably to previously calculated values [24,34–36]. For C-La_2O_3, we determined band gaps of 3.34 and 3.53 eV using LDA and GGA PBE, respectively. We find the band gap of rh-In_2O_3 to be 0.97 eV using GGA PBE and 1.29 eV using LDA, which also agree with previously calculated values [11,27]. For C-In_2O_3, we determine a band gap of 0.94 eV using GGA PBE and 1.18 eV using LDA, which also compare favorably to values previously calculated [11,26,27,29,37]. The band gap values of 2.04 and 2.49 eV using GGA PBE and LDA, respectively, for β-Ga_2O_3 also agree with previously calculated values [29,38]. We determine slightly larger band gap values of 2.75 and 2.25 eV for C-Ga_2O_3 which are comparable to previously calculated values [29].

For all phases and all three sesquioxides, the DOS of the valence band are very similar with O p states dominating the top of the valence band. In and Ga atoms have similar electronegativities and similar electron configurations; hence it is reasonable their oxide band structures are similar. La has a lower electronegativity and, unlike In and Ga which have valence electrons in the s and p shells, La valence electrons occupy the s and d shells. These differences lead to different behavior in the conduction bands of these oxides. In La_2O_3, the bottom of the conduction band is largely made up of d states. The effective mass of an electron is inversely proportional to the second derivative of the conduction band minimum and influences transport properties of a material. In the La_2O_3 band structure [39] the conduction band is broad, resulting in a higher effective mass and low carrier mobility. Contrastingly, the conduction bands in In_2O_3 and Ga_2O_3 are made up of s states spread out over several eV. The conduction band minima in the In_2O_3 [11] and Ga_2O_3 [1] band structures have greater curvature, resulting in a lower effective mass and greater carrier mobility. This property, when combined with the low DOS at the conduction band minimum, allows these materials to remain transparent and semiconducting while La_2O_3 behaves as a *high-k* insulator.

To better understand the stability of the oxides, we calculated the phonon DOS for each oxide in each phase (Fig. 4). As is the case for most metal oxides, we observe that the displacement of metal atoms contributes to the lower-frequency modes and the oxygen atoms contribute to higher-frequency modes. As mentioned previously, C-Ga_2O_3 is not observed in experiment. The phonon DOS contains no imaginary modes; that is, C-Ga_2O_3 is dynamically stable. In all phases of In_2O_3 and La_2O_3, there are distinct regions in which the metal atom

TABLE I. Lattice constants, band gaps, and formation energies of bulk La, In, Ga, La_2O_3, In_2O_3, and Ga_2O_3.

Structure	Method	a (Å)	b (Å)	c (Å)	Band gap (eV)	Formation energy (kJ/mol)
Bulk La	Theory (LDA)	3.534		11.939		
	Theory (GGA PBE)	3.758		12.091		
	Expt. [22]	3.765		12.15 [22]		
C-La_2O_3	Theory (LDA)	11.191			3.34	–1824.2
	Theory (GGA PBE)	11.398			3.53	–1675.9
	Expt.	11.36 [7]				–1793.7 [33]
A-La_2O_3	Theory (LDA)	3.882		5.941	3.74	–1835.0
	Theory (GGA PBE)	3.937		6.179	3.93	–1664.3
	Expt.	3.94 [7]		6.13 [7]	5.5 [53]	–1793.7 [33]
Bulk In	Theory (LDA)	3.174		4.875		
	Theory (GGA PBE)	3.294		5.053		
	Expt.	3.252 [54]		4.947 [54]		
C-In_2O_3	Theory (LDA)	10.069			1.18	–946.6
	Theory (GGA PBE)	10.117			0.94	–774.9
	Expt.	10.126 [40]			3.70 [55,26]	–925.8 [33]
rh-In_2O_3	Theory (LDA)	5.468		14.383	1.29	–935.5
	Theory (GGA PBE)	5.581		14.768	0.97	–751.8
	Expt.	5.491 [40]		14.526 [40]	3.80 [55,26]	–925.8 [33]
Bulk Ga	Theory (LDA)	4.447	4.401	7.512		
	Theory (GGA PBE)	4.543	4.552	7.874		
	Expt. [56]	4.5103	4.4861	7.6463		
C-Ga_2O_3	Theory (LDA)	9.201			2.75	–1230.7
	Theory (GGA PBE)	9.400			2.27	–882.6
	Expt.	10.00 [57]				–1089.1 [33]
β-Ga_2O_3	Theory (LDA)	12.143	3.021	5.761	2.49	–1235.6
	Theory (GGA PBE)	12.445	3.084	5.876	2.04	–899.0
	Expt.	12.22 [58]	3.04 [58]	5.80 [58]	4.7 [55,26]	–1089.1 [33]

or oxygen atom makes a greater contribution to the DOS with little overlap. For example, in rh-In_2O_3, the phonon modes from 0 to ∼7.5 THz are predominantly due to the In atom and modes below ∼7.5 THz are due to the contribution from the O atom. However, in Ga_2O_3, we observe roughly equal contributions of the metal and oxygen states at ∼10 THz. This is prevalent in unstable C-Ga_2O_3 and completely absent in ground state C-In_2O_3. We also observe minimal overlap between metal and oxygen vibrational modes in metastable C-La_2O_3. Perhaps this overlap plays a role in the stabilization of the bixbyite phase.

Next we calculate the phonon contribution to the free energy. The formula used to calculate the free energy is

$$G = U_{\text{Tot}} + U_{\text{vib}} - ST + PV.$$

In this equation, G is the free energy, U_{Tot} is the potential energy which is obtained from the ionic relaxation of the bulk material, U_{vib} is the vibrational energy, S is the phonon entropy, T is temperature, P is pressure, and V is volume. We assume the volume of the cell remains constant,

so the PV term is always equal to 0. Plots of the free energy for all phases of La_2O_3, In_2O_3, and Ga_2O_3 are shown in Fig. 5.

When we consider the harmonic free energy, we may determine a transition temperature at which the A-La_2O_3 phase is predicted to be more stable than the C-La_2O_3 phase. Using GGA PBE, we find at 1070 K the A-La_2O_3 phase is stabilized by the entropic term. While this temperature is lower than the melting temperature of 2577 K [33], clearly, this is a transition temperature that is not observed in experiment since A-La_2O_3 is the more stable polymorph in ambient conditions. Therefore, in this instance GGA PBE does not describe the material properly. Hence, phonons cannot be neglected when using the GGA PBE functional for energetic studies of La_2O_3. The result calculated with the LDA functional predicts that the A-La_2O_3 phase is lower in energy at all temperatures, which agrees with experimental observations. Per formula unit, A-La_2O_3 is lower in energy than C-La_2O_3 by 0.11 eV. Here, we find the phonon contribution to the free energy cannot overcome this difference in
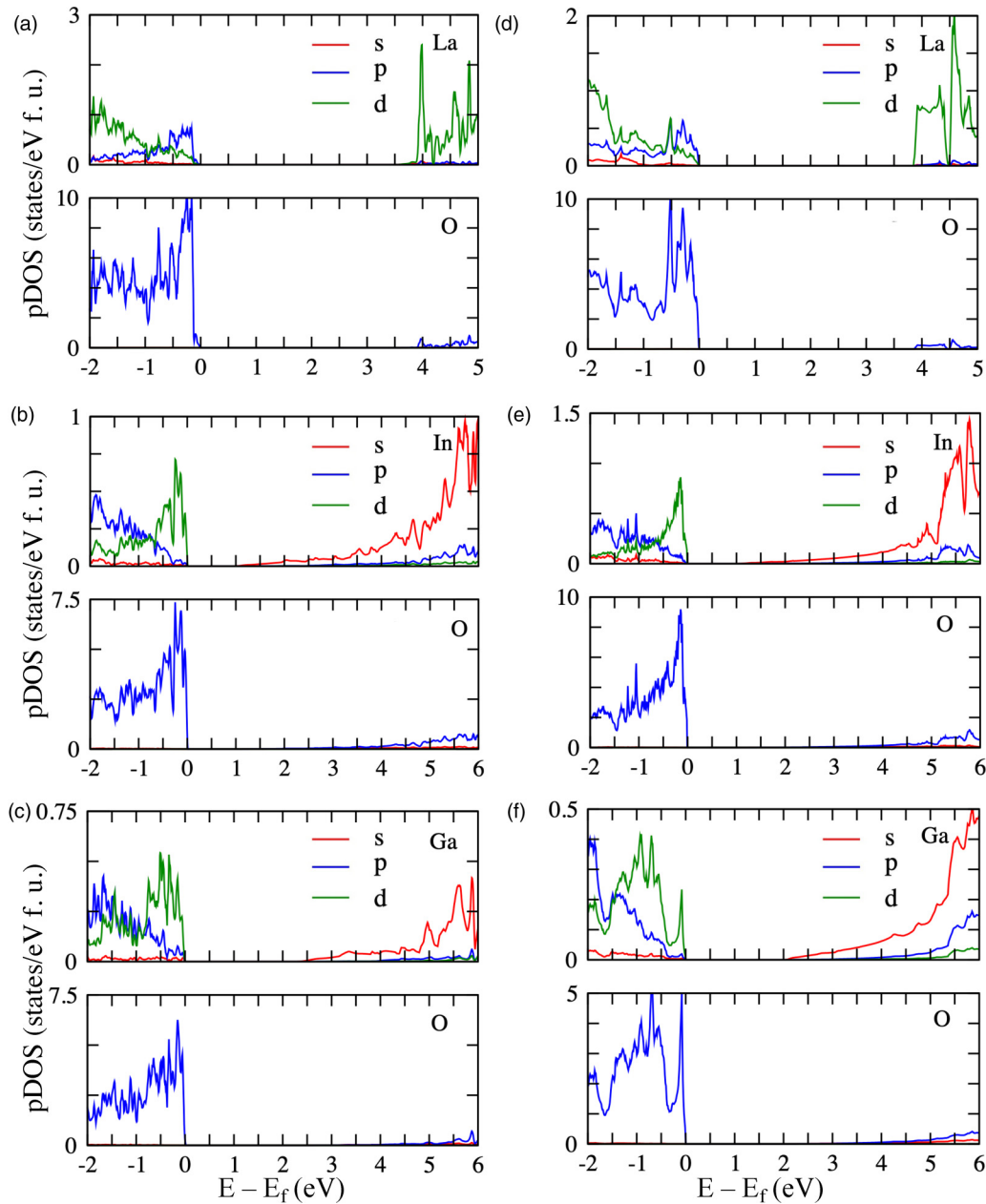
FIG. 2. Density of states per formula unit (f.u.) calculated using GGA PBE for bixbyite (a) La_2O_3, (b) In_2O_3, and (c) Ga_2O_3, and (d) hexagonal La_2O_3, (e) corundum In_2O_3, and (f) monoclinic Ga_2O_3.

total energy between the two phases. Hence, C-La_2O_3 cannot be stabilized simply by high temperatures, as observed in experiment.

The formation energies calculated using both LDA and GGA PBE calculations correctly indicate that the C-In_2O_3 phase is the ground state. Using the free energy, we calculate a transition temperature for the C-In_2O_3 to rh-In_2O_3 transition at 720 K using GGA PBE and a lower transition temperature of 560 K using LDA, both of which are below the In_2O_3 melting point of 1912 K [33]. These temperatures correspond to frequencies of approximately 12 and 15 THz, respectively. Looking at the phonon DOS, it is clear the stabilization of the rh-In_2O_3 phase is due to the vibrational contribution of O atoms at high temperatures. Rh-In_2O_3 is a high-temperature, high-pressure phase. To determine a transition pressure, we

calculated energy vs volume for both phases of In_2O_3 (Fig. 6) and determined the transition pressure by interpolating the tangent between the minima of both curves. For a direct transition between the bixbyite and corundum phases, we determine a transition pressure of 13.9 GPa using GGA PBE and 11.0 GPa using LDA. These values agree well with previously determined theoretical values using GGA PBE [40]. In experiment, the phase transition to rh-In_2O_3 requires an increase in both pressure and temperature [28,40]; hence we cannot directly compare our results to experiment. This indicates that in order to sufficiently lower the energy and stabilize the corundum phase, changes to both the total energy and entropy are required to undergo a phase transition. An increase in pressure is necessary to decrease the bond lengths which results in larger splitting between electronic states. This allows
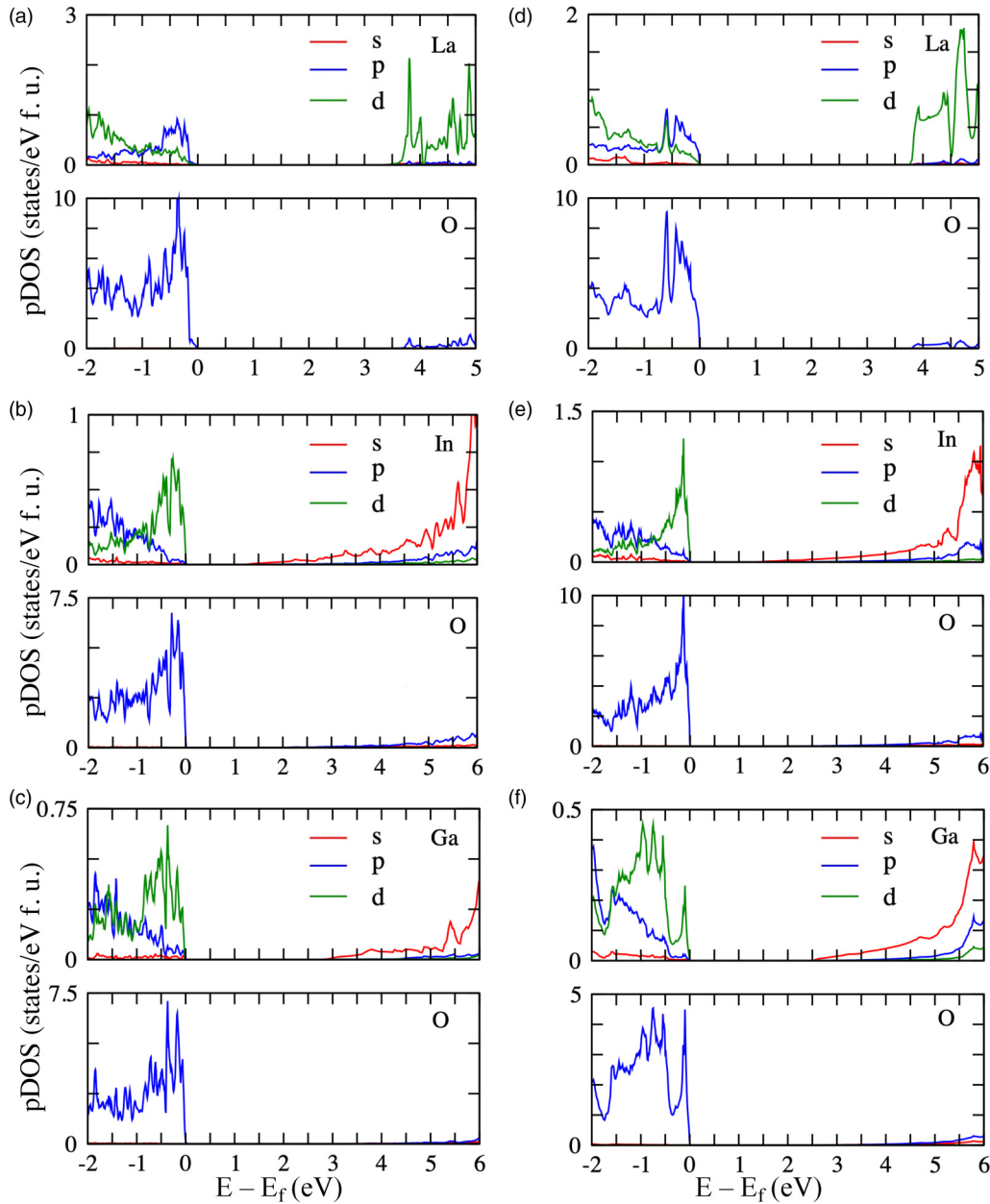

FIG. 3. Density of states calculated using LDA for bixbyite (a) La_2O_3, (b) In_2O_3, and (c) Ga_2O_3, and (d) hexagonal La_2O_3, (e) corundum In_2O_3, and (f) monoclinic Ga_2O_3.

electrons to occupy lower-energy states and decreases the total energy. An increase in temperature will lower free energy by increasing the magnitude of the $-S\Delta T$ term. Experimentally, the rh-In_2O_3 phase is observed at pressures as low as 6.5 GPa and up to 14 GPa [28,40]. The theoretical transition pressures we have calculated are higher than those observed in experiment likely because we need to consider both temperature and pressure.

Our calculations using both LDA and GGA PBE predict that the β-Ga_2O_3 phase is the ground state. Considering the free energy, we found that GGA PBE predicts a transition temperature of 2870 K, which is far above the Ga_2O_3 melting point of 1807 K [33], and LDA predicts that the bixbyite phase is always less stable than β-Ga_2O_3, which agrees with experimental observations [1]. Similar to what we have found

for C-La_2O_3, our results show the phonon contribution to the free energy is not enough to overcome the difference in the internal energy between the bixbyite and monoclinic phases. Hence, high-temperature conditions will not stabilize C-Ga_2O_3.

B. Surface properties

Next, we look at the surface energies for several low-index terminations of the various La_2O_3, In_2O_3, and Ga_2O_3 phases. For the bixbyite structures, we looked at the (001), (011), and (111) surfaces. We looked at two possible terminations of the (001) surface in which the surface is either terminated with the metal or oxygen atoms. For both hexagonal La_2O_3 and corundum In_2O_3 we looked at the (001), (110), (100), and

FIG. 4. Phonon density of states for ground state and metastable structures of (a) La$_2$O$_3$, (b) In$_2$O$_3$, and (c) Ga$_2$O$_3$ calculated using LDA, and bixbyite (d) La$_2$O$_3$, (e) In$_2$O$_3$, and (f) Ga$_2$O$_3$ calculated using GGA PBE.

($1\bar{1}2$) surface terminations, which correspond to the c, m, a, and r planes, respectively. For monoclinic Ga$_2$O$_3$, we studied the (100), ($11\bar{2}$), ($\bar{2}01$), (310), and (101) surfaces. For each slab, the top and bottom surfaces were chosen such that they are equivalent. For slabs that have inversion symmetry, we were able to create a stoichiometric slab with equivalent top and bottom surfaces and for slabs without inversion symmetry, we created nonstoichiometric slabs.

Following the formalism outlined in Ref. [41], the surface energy for stoichiometric slabs is calculated using the

equation

$$\Upsilon_{\text{surface}} = \frac{1}{2A}[E_{\text{slab}} - N_{M_2O_3}E_{M_2O_3}].$$

Here, $\Upsilon_{\text{surface}}$ is the surface energy, A is the surface area with a factor of 2 accounting for the top and bottom surfaces, E_{slab} is the energy of the sesquioxide slab, $N_{M_2O_3}$ is the number of bulk sesquioxide units, and $E_{M_2O_3}$ is the energy of the bulk sesquioxide. For slabs that do not possess inversion symmetry, we need to use the chemical potential to calculate the surface
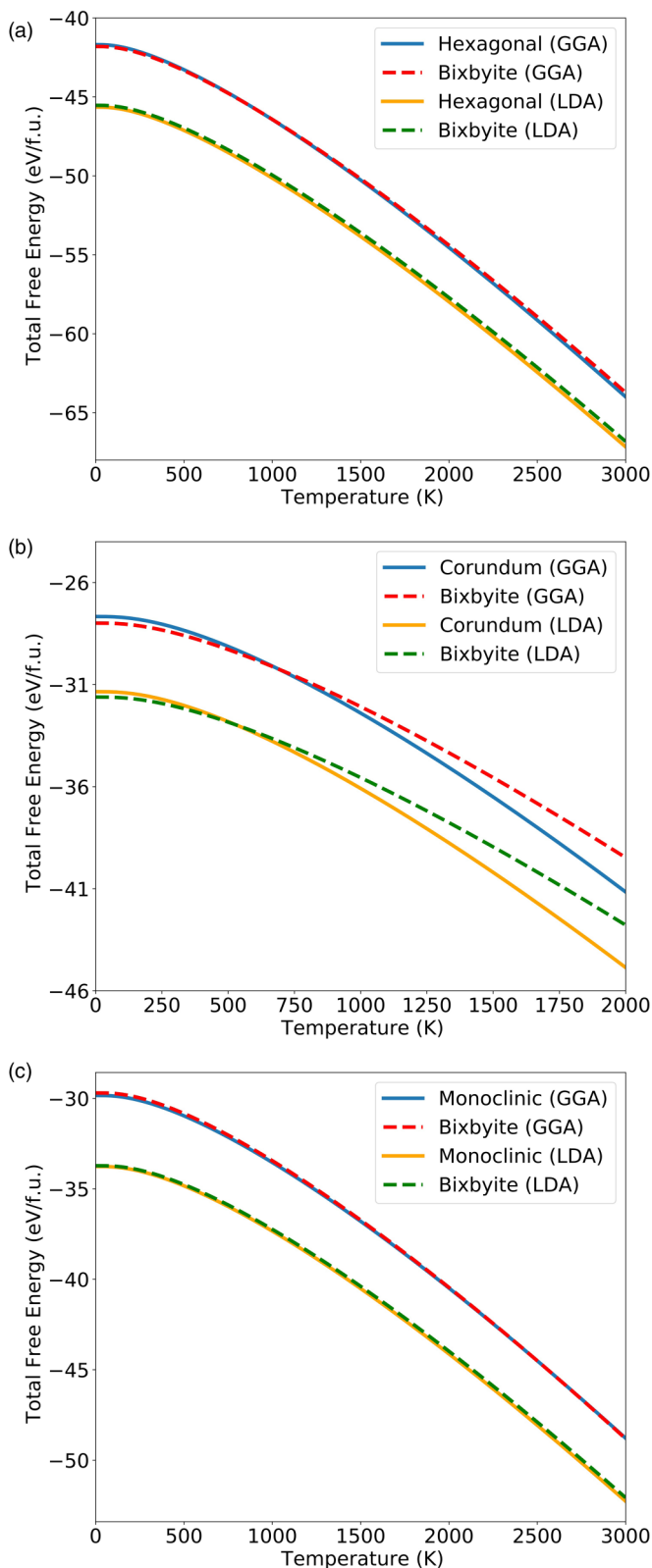
FIG. 5. Free energy plots of (a) La_2O_3, (b) In_2O_3, and (c) Ga_2O_3.

FIG. 6. Energy vs volume plots for bulk bixbyite and corundum In_2O_3 using (a) LDA and (b) GGA PBE.

In this equation, N_M (N_O) is the number of metal (oxygen) atoms in the slab, E_M (E_O) is the energy of one unit cell of bulk metal (molecular O_2), and μ_M (μ_{O_2}) is the chemical potential of bulk metal (molecular O_2). To simplify the number of variables in this equation, we use the following relationship:

$$E_{M_2O_3} + \mu_{M_2O_3} = 2(E_{Ga} + \mu_{Ga}) + \frac{3}{2}(E_{O_2} + \mu_{O_2}).$$

We assume that the surface is in equilibrium with its own bulk; hence $\mu_{M_2O_3}$ is equal to 0 eV. The formation energy of M_2O_3 is defined as $E_f = E_{M_2O_3} - 2E_M - \frac{3}{2}E_{O_2}$. Using this definition and rearranging the previous equation, we get the relationship $\mu_M = \frac{1}{2}(E_f - \frac{3}{2}\mu_{O_2})$. We can then allow the chemical potential to vary over the range $0 \leqslant \mu_{O_2} \leqslant \frac{2}{3}E_f$, where $\mu_{O_2} = 0$ eV represents oxygen-rich conditions and $\mu_{O_2} = \frac{2}{3}E_f$ represents metal-rich conditions.

The surface energies for all three sesquioxides in the bixbyite phase are listed in Table II. For all three sesquioxides, both LDA and GGA PBE predict that the lowest-energy surface termination is the (111) termination and the highest-energy surface is metal terminated (001). Despite differences in the ionic radii, electronegativity of the metal atoms, and stability of the bixbyite phase, the three compounds show the same trend in highest to lowest surface energy terminations and even similar surface energy values. There have been few, if any previous reports on the surface energy of bixbyite Ga_2O_3 or La_2O_3; however, previous studies on In_2O_3 have indicated the same trend we have observed [42,43]. Of the three surface terminations we have studied for the bixbyite

energy using the following equation:

$$\Upsilon_{surface} = \frac{1}{2A}\left[E_{slab} - N_M(E_M + \mu_M) - \frac{1}{2}N_O(E_{O_2} + \mu_{O_2})\right].$$

TABLE II. Surface energies (J/m^2) for bixbyite La$_2$O$_3$, In$_2$O$_3$, and Ga$_2$O$_3$ calculated using GGA PBE and LDA. All slabs used are stoichiometric.

		Surface	Termination	Surface energy before relaxation	Surface energy after relaxation	Relaxation energy
La$_2$O$_3$	GGA PBE	(001)	La	2.747	1.733	1.014
		(001)	O	2.345	1.274	1.071
		(011)	Mixed	1.114	0.758	0.355
		(111)	Mixed	0.902	0.614	0.288
	LDA	(001)	La	2.583	1.525	1.057
		(001)	O	3.331	1.446	1.885
		(011)	Mixed	1.389	0.997	0.393
		(111)	Mixed	1.140	0.819	0.321
In$_2$O$_3$	GGA PBE	(001)	In	2.848	2.108	0.740
		(001)	O	2.451	1.840	0.610
		(011)	Mixed	1.440	1.099	0.341
		(111)	Mixed	1.097	0.776	0.321
	LDA	(001)	In	3.289	2.310	0.979
		(001)	O	2.973	2.249	0.724
		(011)	Mixed	1.737	1.397	0.340
		(111)	Mixed	1.519	1.153	0.366
Ga$_2$O$_3$	GGA PBE	(001)	Ga	3.266	1.700	1.566
		(001)	O	3.397	1.564	1.833
		(011)	Mixed	1.670	1.053	0.617
		(111)	Mixed	0.788	0.711	0.077
	LDA	(001)	Ga	3.962	2.355	1.607
		(001)	O	4.131	2.295	1.836
		(011)	Mixed	2.109	1.474	0.636
		(111)	Mixed	1.639	1.065	0.574

phase, the (111) plane has the greatest planar density which reduces the surface energy by breaking fewer bonds at the surface. In bulk bixbyite, the metal and oxygen atoms are six- and fourfold coordinated. We see a small reduction in coordination at the (111) surface. After relaxation, the metal atoms are five- and sixfold coordinated while the O atoms are threefold coordinated. Contrastingly, the metal atoms at the (100) metal-terminated surface reduce to three- and fourfold coordinated while one-third of the O atoms are threefold coordinated and the remaining two-thirds are fourfold coordinated. While most of the surface O atoms resemble bulk O, the significant reduction in coordination of the metal atoms destabilizes the surface.

The surface energies we have calculated for rh-In$_2$O$_3$ are shown in Table III. We find the lowest-energy surface terminations predicted by LDA and GGA PBE vary. LDA predicts the lowest-energy surface termination is (11$\bar{2}$) [Fig. 7(a)] while GGA PBE predicts it is (001) [Fig. 8(a)]. Despite having a relatively low surface energy, the (001) surface showed the greatest reduction in coordination. In reduced from sixfold coordinated in bulk rh-In$_2$O$_3$ to threefold coordinated at the (001) surface while the O atoms reduce from four- to threefold coordinated. Additionally, the (11$\bar{2}$) and (110) surfaces have relatively low and high surface energies, respectively, but both have five- and threefold coordinated In and O atoms at the surface, showing there is no clear relationship between coor-

dination and surface stability in rh-In$_2$O$_3$. When comparing rh- and C-In$_2$O$_3$, GGA PBE predicts that the lowest-energy surface termination is the (001) rh-In$_2$O$_3$ surface while LDA predicts (111) C-In$_2$O$_3$ is the lowest-energy surface. If the (001) rh-In$_2$O$_3$ surface is indeed lower in energy, we expect to experimentally observe the corundum phase in the early stages of In$_2$O$_3$ crystal growth, below some critical thickness. The existence of rh-In$_2$O$_3$ during the growth of In$_2$O$_3$ has been observed in the growth of In$_2$O$_3$ nanocrystals smaller than 5 nm [44], while no such observation is reported in the growth of In$_2$O$_3$ nanotowers [45], nanocrystals [46,47], or thin films [48]. Given the varying experimental observations, we cannot definitively state whether the surface energies calculated using the LDA or the GGA PBE functional better correspond to what is observed in experiment.

As mentioned previously, we studied the (100), (11$\bar{2}$), ($\bar{2}$01), (310), and (101) surfaces of β-Ga$_2$O$_3$. The surface energies for all terminations are listed in Table IV and the lowest-energy terminations are shown in Figs. 7(b) and (8b). To determine the lowest-energy surface reconstruction of the (100) plane, we study two stoichiometric, mixed-terminated surfaces. Using GGA PBE, we found that the surface energy of the A termination is 0.774 J m^{-2}, which is higher than the surface energy value of 0.459 J m^{-2} for the B termination. The surface energy values we have calculated are lower than the values reported by Bermudez [49]. However, we find that

TABLE III. Surface energies (J/m^2) for rh-In$_2$O$_3$ calculated using GGA PBE and LDA. All slabs used are stoichiometric with mixed terminations.

	Surface	Surface energy before relaxation	Surface energy after relaxation	Relaxation energy
GGA PBE	(001)	1.393	0.634	0.758
	(110)	1.444	1.073	0.370
	(1$\bar{1}$2)	1.191	0.938	0.253
	(100)	1.764	1.153	0.610
LDA	(001)	2.345	1.422	0.923
	(110)	1.864	1.593	0.271
	(1$\bar{1}$2)	1.601	1.371	0.229
	(100)	4.048	1.682	2.366

TABLE IV. Surface energies (J/m^2) for β-Ga$_2$O$_3$ calculated using GGA PBE and LDA.

|	Surface	Termination	Environment (Ga- or O-rich)	Surface energy before relaxation	Surface energy after relaxation	Relaxation energy
GGA PBE	($\bar{2}$01)	Ga (A)	Ga	1.320	1.204	0.116
			O	4.554	4.438	
	($\bar{2}$01)	O (A)	Ga	7.347	5.212	2.135
			O	4.113	1.978	
	($\bar{2}$01)	Ga (B)	Ga	1.276	1.211	0.065
			O	4.510	4.445	
	($\bar{2}$01)	O (B)	Ga	7.268	7.014	0.254
			O	4.034	3.780	
	($\bar{2}$01)	Mixed	–	2.100	0.768	1.332
	(310)	Ga	Ga	1.796	1.472	0.324
			O	6.194	5.870	
	(310)	O	Ga	9.618	6.466	3.151
			O	5.219	2.068	
	(101)	Mixed	–	2.724	1.573	1.150
	(101)	O	–	3.431	1.510	1.920
	(100)-A	Mixed	–	1.264	0.774	
	(100)-B	Mixed	–	0.688	0.459	0.490
	($\bar{1}$12)	Mixed	Ga	4.919	3.976	0.229
			O	2.933	1.990	0.943
LDA	($\bar{2}$01)	Ga (A)	Ga	1.762	1.631	0.130
			O	6.408	6.277	
	($\bar{2}$01)	O (A)	Ga	8.585	6.054	2.531
			O	3.939	1.408	
	($\bar{2}$01)	Ga (B)	Ga	1.774	1.654	0.120
			O	6.420	6.300	
	($\bar{2}$01)	O (B)	Ga	8.376	7.040	1.336
			O	3.730	2.394	
	($\bar{2}$01)	Mixed	–	2.743	1.131	1.612
	(310)	Ga	Ga	2.402	2.102	0.300
			O	8.700	8.400	
	(310)	O	Ga	11.117	7.536	3.581
			O	4.819	1.238	
	(101)	Mixed	–	3.314	1.999	1.316
	(101)	O	–	4.098	2.059	2.039
	(100)-A	Mixed	–	1.156	0.943	0.212
	(100)-B	Mixed	–	1.566	1.451	0.116
	($\bar{1}$12)	Mixed	Ga	10.492	7.432	3.061
			O	4.764	1.703	
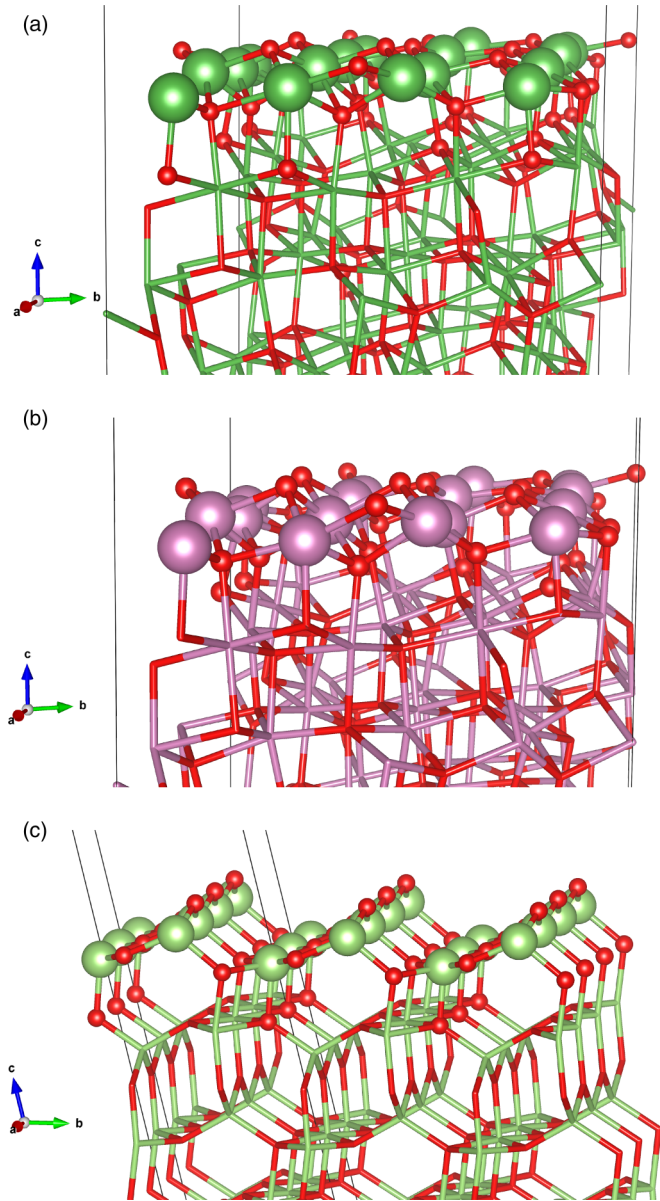
FIG. 7. Lowest-energy surface terminations calculated using LDA; (a) La_2O_3 (111), (b) In_2O_3 (111), (c) Ga_2O_3 (100)-*A*.

FIG. 8. Lowest-energy surface terminations calculated using GGA PBE; (a) La_2O_3 (111), (b) In_2O_3 (0001), (c) Ga_2O_3 (100)-*B*.

the difference in energy between the (100)-*A* and (100)-*B* terminations is 0.315 J m^{-2}, which is comparable to the energy difference of 0.45 J m^{-2} between the two terminations reported by Bermudez. Using LDA, we determined the surface energy of the (100)-*A* termination is 0.906 J m^{-2} which is lower than the surface energy of the (100)-*B* termination, 1.393 J m^{-2}. The difference in surface energy is 0.487 J m^{-2}, which remains comparable to the difference we calculated using GGA PBE and that reported by Bermudez. For the ($\bar{1}12$) plane, we study one nonstoichiometric, mixed-terminated surface. Using GGA PBE, we find the surface energy is 3.976 J m^{-2} under Ga-rich conditions and 1.990 J m^{-2} under O-rich conditions, indicating the surface is more stable in O-rich conditions. Using LDA, we determine the surface energy is 1.625 and 7.089 J m^{-2} under Ga- and O-rich conditions, respectively, indicating the surface is more stable under Ga-rich

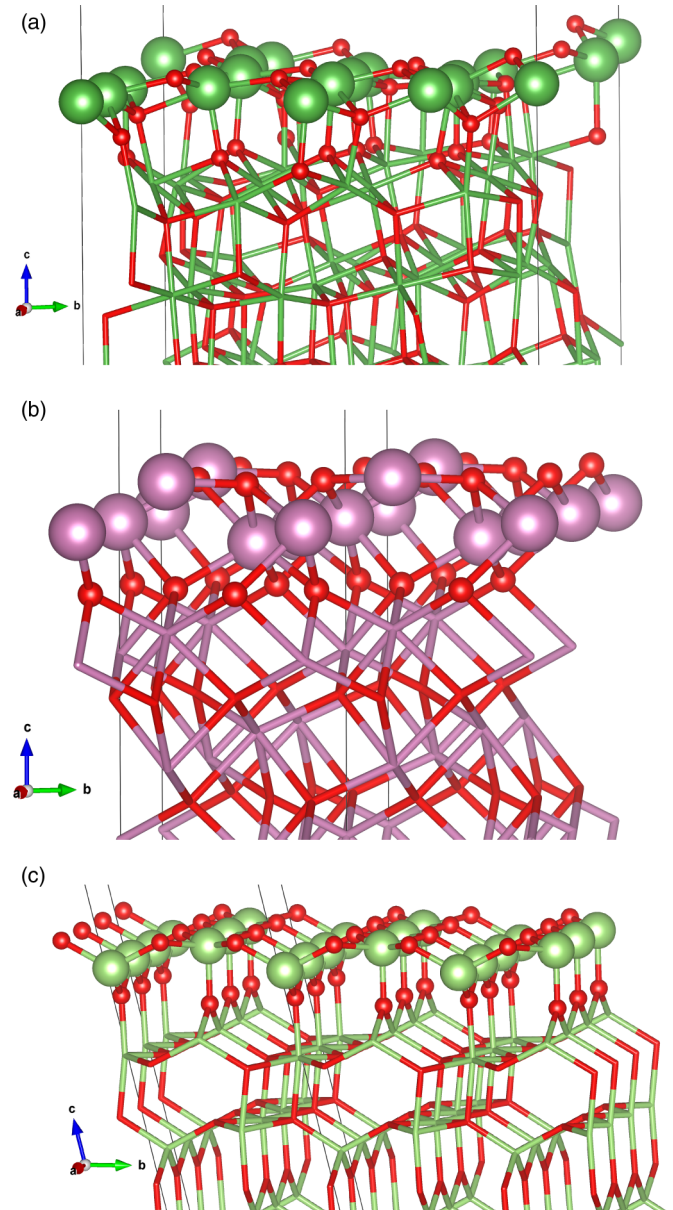conditions. There are few previous reports of surface energy calculations for the ($\bar{1}12$) surface termination. To determine the lowest-energy surface reconstruction of the ($\bar{2}01$) surface, we studied five surface terminations: two distinct Ga terminations, two distinct O terminations, and one mixed termination. The lowest value for the surface energy is 0.768 J m^{-2} using GGA PBE and 1.083 J m^{-2} using LDA, which was achieved with the mixed termination in both calculations. Although a different calculation method was used, the surface energy and relaxation energy we have determined is comparable to the values reported by Schewski *et al.* [50]. For the (310) surface, we studied one Ga-terminated and one O-terminated surface using nonstoichiometric slabs. The calculation using GGA PBE predicts the lowest-energy surface termination is achieved with a Ga-terminated surface under Ga-rich conditions and has a surface energy of 1.472 J m^{-2}. Conversely,

TABLE V. Surface energies (J/m^2) for A-La_2O_3 calculated using GGA PBE and LDA. All slabs have mixed terminations.

	Surface	Environment (La- or O-rich)	Surface energy before relaxation	Surface energy after relaxation	Relaxation energy
GGA PBE	(001)	–	0.637	0.629	0.008
	(110)	–	1.322	0.949	0.373
	(1$\bar{1}$2)	–	1.149	0.781	0.368
	(100)	La	1.780	1.109	0.672
		O	3.200	2.529	
LDA	(001)	–	1.021	0.920	0.101
	(110)	–	1.640	1.259	0.381
	(1$\bar{1}$2)	–	1.511	1.102	0.409
	(100)	La	2.111	1.355	0.756
		O	3.762	3.007	

the calculation using LDA predicts the lowest-energy surface termination is achieved with an O-terminated surface under O-rich conditions. To study the (101) surface, we studied a mixed-terminated surface and an O-terminated surface. Using GGA PBE, the surface energy for the O-terminated surface is $1.510\,J\,m^{-2}$, which is slightly lower than the surface energy of $1.573\,J\,m^{-2}$ for the mixed-terminated surface. The values we have calculated are comparable to the surface energy value of 1.5–$2\,J\,m^{-2}$ reported by Schewski *et al.* [50]. Overall, LDA and GGA PBE predict (100)-A and (100)-B are the lowest-energy surface terminations.

In both (100)-A and (100)-B surfaces, we see the Ga1 atom remains fourfold coordinated and the Ga2 atom was reduced from six- to fivefold coordinated. The O3 atom at the surface remains threefold coordinated while the coordination of the O1 atom in (100)-B reduces from 3 to 4 and in the O2 atom in (100)-A it reduces from 2 to 3. Overall, we see only a slight reduction in the coordination of surface atoms. In the less stable surfaces, such as O-terminated (310) and O-terminated ($\bar{2}$01)-B, we see a very similar change in coordination of the Ga and O atoms as observed for the (100) surfaces; however, the number of unsaturated bonds has increased at the (310) and ($\bar{2}$01)-B due to the greater number of atoms at the surface. The surfaces are destabilized by the greater number of bonds broken to create these surfaces and the greater number of atoms that experience a reduced coordination.

The surface energies for A-La_2O_3 are listed in Table V. We see that both LDA and GGA PBE predict the (001) termination is the lowest energy [Figs. 7(c) and 8(c)] and the energy we have determined is comparable to previously reported values [51]. At this surface, the La atoms are sixfold coordinated, slightly lower than the sevenfold coordinated La in bulk A-La_2O_3. The coordination of the O atoms at this surface also slightly reduced from fourfold to threefold coordinated. The (100) termination is the least stable and we find that, while the La atoms remain sevenfold coordinated, the significant reduction of O atoms from sixfold to twofold coordination destabilized the surface.

When comparing C- and A-La_2O_3, GGA PBE predicts that the (111) C-La_2O_3 surface is lower in energy than the (001) A-La_2O_3 surface by only $0.015\,J/m^{-2}$ whereas LDA predicts the (111) surface is lower by $0.101\,J/m^{-2}$. The ground state structure of La_2O_3 is the hexagonal phase, but the lowest-energy termination is the (111) surface of C-La_2O_3. This

suggests that there may be a thickness at which the low surface energy of the metastable C-La_2O_3 dominates the low energy of bulk A-La_2O_3, called the critical thickness, which has been previously observed in metastable phases of hafnia [52].

Since LDA predicts the correct ground state structure, we calculate the critical thickness using the surface energies we calculated using LDA. If we assume the interfacial energy between C- or A-La_2O_3 and the substrate are the same, the critical thickness can be estimated using the following equation,

$$h = \frac{\gamma_{A\text{-}La_2O_3}^{\text{surface}} - \gamma_{C\text{-}La_2O_3}^{\text{surface}}}{E_{C\text{-}La_2O_3}^{coh} - E_{A\text{-}La_2O_3}^{coh}},$$

where $\gamma_{X\text{-}La_2O_3}^{\text{surface}}$ and $E_{X\text{-}La_2O_3}^{coh}$ are the surface energy and cohesive energy of C- or A-La_2O_3. Using the surface energies of (111) C-La_2O_3 and (001) A-La_2O_3, we calculate a critical thickness of 1.5 Å, which is much smaller than the critical thickness of at least 5 nm observed in experiment [7,8]. Additionally, a height of 1.5 Å does not form a full unit cell of either C- or A-La_2O_3, meaning this theoretical prediction is nonphysical. If we now consider that the interfacial energy is not equal, we can calculate the difference in the interfacial energy using the equation

$$E_{A\text{-}La_2O_3}^{\text{Interface}} - E_{C\text{-}La_2O_3}^{\text{Interface}} = h\big(E_{C\text{-}La_2O_3}^{coh} - E_{A\text{-}La_2O_3}^{coh}\big) \\ + \gamma_{A\text{-}La_2O_3}^{\text{surface}} - \gamma_{C\text{-}La_2O_3}^{\text{surface}},$$

where $E_{X\text{-}La_2O_3}^{\text{Interface}}$ is the interfacial energy between C- or A-La_2O_3 and the substrate. If we consider the smallest experimentally observed experimental thickness of 5 nm, the interfacial energy of A-La_2O_3 is higher than that of C-La_2O_3 by $3.45\,eV/Å^2$. Considering the largest experimentally observed critical thickness of 15 nm, the interfacial energy of A-La_2O_3 is higher by $10.33\,eV/Å^2$. While the surface energy of (111) C-La_2O_3 is lower than that of (0001) A-La_2O_3, our calculations show that the interfacial energy likely predominantly drives the stabilization of the C-La_2O_3 phase during the early stages of film growth rather than the surface energy alone.

IV. CONCLUSIONS

In this work, we have investigated the bulk and surface properties of La_2O_3, In_2O_3, and Ga_2O_3. We determined that

although we can calculate lattice constants closer to the experimental values using the GGA PBE functional, the correct ground state structure for La_2O_3 is predicted only using the LDA functional. This incorrect prediction was remedied by including the entropic contribution with respect to temperature and we determined a transition temperature of 1070 K. Hence, the GGA PBE functional could be used when investigating structural properties of La_2O_3, but the LDA functional should be used when measuring energetic properties.

We determined theoretical C-In_2O_3 to rh-In_2O_3 transition temperatures and pressures of 560 K and 11.0 GPa using LDA, and 720 K and 13.9 GPa using GGA PBE. Using the GGA PBE functional, we find the C-Ga_2O_3 phase is stable at temperatures above 2870 K, which is much higher than the Ga_2O_3 melting point of 1807 K [33]. On the other hand, our calculations using LDA predict that the monoclinic phase remains more stable at high temperatures, which agrees with experimental observations.

We determined the lowest-energy surface terminations for La_2O_3, In_2O_3, and Ga_2O_3 and any inconsistencies between the lowest-energy surface determined using LDA or GGA PBE functionals. The surface energies for La_2O_3 and In_2O_3 using LDA and GGA PBE are comparable; however, the predicted surface terminations for β-Ga_2O_3 are more sensitive to functional choice. We also determined a theoretical critical thickness of 1.5 Å to observe metastable bixbyite La_2O_3, which is much lower than the experimentally determined critical thickness of at least 5 nm. Using the experimental critical thickness, we determined that the interfacial energy of A-La_2O_3 is higher than that of C-La_2O_3 by 3.45 eV/$Å^2$, indicating that the interfacial energy drives the formation of metastable bixbyite La_2O_3 in film growth.

[1] J. Zhang, J. Shi, D. C. Qi, L. Chen, and K. H. L. Zhang, APL Mater. **8**, 020906 (2020).

[2] L. N. Liu, W. M. Tang, and P. T. Lai, Coatings **9**, 217 (2019).

[3] R. S. Gedam and D. D. Ramteke, J. Phys. Chem. Solids **74**, 1039 (2013).

[4] K. Yoshimoto, A. Masuno, M. Ueda, H. Inoue, H. Yamamoto, and T. Kawashima, J. Am. Ceram. Soc. **101**, 3328 (2018).

[5] X. Huang, D. Zhao, L. Ma, C. Deng, L. Li, K. Chen, and X. Yang, J. Non-Cryst. Solids **536**, 120007 (2020).

[6] P. Pisecny, K. Husekova, K. Frohlich, L. Harmatha, J. Soltys, D. Machajdik, J. P. Espinos, M. Jergel, and J. Jakabovic, Mater. Sci. Semicond. Process. **7**, 231 (2004).

[7] P.-Y. Chen, T. Hadamek, S. Kwon, F. Al-Quaiti, A. B. Posadas, M. J. Kim, A. A. Demkov, and J. G. Ekerdt, J. Vac. Sci. Technol. A **38**, 012403 (2020).

[8] A. Proessdorf, M. Niehle, M. Hanke, F. Grosse, V. Kaganer, O. Bierwagen, and A. Trampert, Appl. Phys. Lett. **105**, 021601 (2014).

[9] J. S. Jur, V. D. Wheeler, D. J. Lichtenwalner, J. P. Maria, and M. A. L. Johnson, Appl. Phys. Lett. **98**, 042902 (2011).

[10] O. Bierwagen, Semicond. Sci. Technol. **30**, 24001 (2015).

[11] T. de Boer, M. F. Bekheet, A. Gurlo, R. Riedel, and A. Moewes, Phys. Rev. B **93**, 155205 (2016).

[12] D. Chu, Y. P. Zeng, D. Jiang, and J. Xu, Nanotechnology **18**, 435605 (2007).

[13] B. Yaglioglu, H. Y. Yeom, and D. C. Paine, Appl. Phys. Lett. **86**, 261908 (2005).

[14] C. Y. Wang, Y. Dai, J. Pezoldt, B. Lu, T. Kups, V. Cimalla, and O. Ambacher, Cryst. Growth Des. **8**, 1257 (2008).

[15] C. H. Lee, M. Kim, T. Kim, A. Kim, J. Paek, J. W. Lee, S. Y. Choi, K. Kim, J. B. Park, and K. Lee, J. Am. Chem. Soc. **128**, 9326 (2006).

[16] Y. B. Lu, Y. H. Li, Z. C. Ling, W. Y. Cong, P. Zhang, Y. Q. Xin, and T. L. Yang, J. Phys. D: Appl. Phys. **49**, 065105 (2016).

[17] R. Roy, V. G. Hill, and E. F. Osborn, J. Am. Chem. Soc. **74**, 719 (1952).

[18] M. Zinkevich and F. Aldinger, J. Am. Ceram. Soc. **87**, 683 (2004).

[19] G. Kresse and J. Furthmüller, Phys. Rev. B **54**, 11169 (1996).

[20] P. E. Blöchl, Phys. Rev. B **50**, 17953 (1994).

[21] A. Togo and I. Tanaka, Scr. Mater. **108**, 1 (2015).

[22] C. Wei, J. L. Fan, and H. R. Gong, J. Alloys Compd. **618**, 615 (2015).

[23] S. Wang, L. Cong, C. Zhao, Y. Li, Y. Pang, Y. Zhao, S. Li, and Y. Sun, Phys. Chem. Chem. Phys. **19**, 26799 (2017).

[24] L. Marsella and V. Fiorentini, Phys. Rev. B **69**, 172103 (2004).

[25] P. Delugas, V. Fiorentini, and A. Filippetti, Phys. Rev. B **80**, 104301 (2009).

[26] S. Z. Karazhanov, P. Ravindran, P. Vajeeston, A. Ulyashin, T. G. Finstad, and H. Fjellvåg, Phys. Rev. B **76**, 075129 (2007).

[27] F. Fuchs and F. Bechstedt, Phys. Rev. B **77**, 155107 (2008).

[28] B. García-Domene, J. A. Sans, F. J. Manjón, S. V. Ovsyannikov, L. S. Dubrovinsky, D. Martinez-Garcia, O. Gomis, D. Errandonea, H. Moutaabbid, Y. Le Godec, H. M. Ortiz, A. Muñoz, P. Rodríguez-Hernández, and C. Popescu, J. Phys. Chem. C **119**, 29076 (2015).

[29] F. P. Sabino, R. Besse, L. N. Oliveira, S. H. Wei, and J. L. F. Da Silva, Phys. Rev. B **92**, 205308 (2015).

[30] J. L. Lyons, ECS J. Solid State Sci. Technol. **8**, Q3226 (2019).

[31] H. Peelaers, D. Steiauf, J. B. Varley, A. Janotti, and C. G. Van de Walle, Phys. Rev. B **92**, 085206 (2015).

[32] M. D. Santia, N. Tandon, and J. D. Albrecht, Solid State Commun. **297**, 1 (2019).

[33] D. R. Lide, *CRC Handbook of Chemistry and Physics*, 85th ed. (CRC Press, Boca Raton, FL, 2004).

[34] K. Xiong and J. Robertson, Microelectron. Eng. **86**, 1672 (2009).

[35] H. Jiang, P. Rinke, and M. Scheffler, Phys. Rev. B **86**, 125115 (2012).

[36] N. Singh, S. M. Saini, T. Nautiyal, and S. Auluck, J. Appl. Phys. **100**, 083525 (2006).

[37] H. Odaka, Y. Shigesato, T. Murakami, and S. Iwata, Jpn. J. Appl. Phys. **40**, 3231 (2001).

[38] K. Yamaguchi, Solid State Commun. **131**, 739 (2004).

[39] P. W. Peacock and J. Robertson, J. Appl. Phys. **92**, 4712 (2002).

[40] A. Gurlo, P. Kroll, and R. Riedel, Chem. Eur. J. **14**, 3306 (2008).

[41] X. Zhang and A. A. Demkov, J. Vac. Sci. Technol. B **20**, 1664 (2002).

[42] P. Agoston and K. Albe, Phys. Rev. B **84**, 045311 (2011).

[43] A. Walsh and C. R. A. Catlow, J. Mater. Chem. **20**, 10438 (2010).

[44] S. S. Farvid, N. Dave, and P. V. Radovanovic, Chem. Mater. **22**, 9 (2010).

[45] Y.-G. Yan, Y. Zhang, H.-B. Zeng, and L.-D. Zhang, Cryst. Growth Des. **7**, 940 (2007).

[46] Z. Galazka, R. Uecker, K. Irmscher, D. Schulz, D. Klimm, M. Albrecht, M. Pietsch, S. Ganschow, A. Kwasniewski, and R. Fornari, J. Cryst. Growth **362**, 349 (2013).

[47] N. Imanaka, T. Masui, Y. W. Kim, and G. Y. Adachi, J. Cryst. Growth **264**, 134 (2004).

[48] A. R. Kirmani, H. Chen, C. M. Stafford, E. G. Bittle, and L. J. Richter, Adv. Electron. Mater. **6**, 2000354 (2020).

[49] V. M. Bermudez, Chem. Phys. **323**, 193 (2006).

[50] R. Schewski, K. Lion, A. Fiedler, C. Wouters, A. Popp, S. V. Levchenko, T. Schulz, M. Schmidbauer, S. Bin Anooz, R. Grüneberg, Z. Galazka, G. Wagner, K. Irmscher, M. Scheffler, C. Draxl, and M. Albrecht, APL Mater. **7**, 022515 (2019).

[51] C. Wei, Q. Q. Ren, J. L. Fan, and H. R. Gong, J. Nucl. Mater. **466**, 234 (2015).

[52] R. Batra, H. D. Tran, and R. Ramprasad, Appl. Phys. Lett. **108**, 172902 (2016).

[53] A. Debernardi, AIMS Mater. Sci. **2**, 279 (2015).

[54] O. Schulte and W. B. Holzapfel, Phys. Rev. B **48**, 767 (1993).

[55] H. H. Tippins, Phys. Rev. **140**, A316 (1965).

[56] V. Heine, J. Phys. C: Solid State Phys. **1**, 222 (1968).

[57] S. I. Stepanov, V. I. Nikolaev, V. E. Bougrov, and A. E. Romanov, Rev. Adv. Mater. Sci. **44**, 63 (2016).

[58] H. Y. Playford, A. C. Hannon, E. R. Barney, and R. I. Walton, Chem. Eur. J. **19**, 2803 (2013).